Ocean and Coastal Management 153 (2018) 193–202

Contents lists available at ScienceDirect

Ocean and Coastal Management

journal homepage: www.elsevier.com/locate/ocecoaman

Assessing 'coastal squeeze' of wetlands at the Yellow River Delta in China: A case study

Shuxin Luo[a], Dongdong Shao[a,*], Wei Long[b], Yajiao Liu[a], Tao Sun[a], Baoshan Cui[a]

[a] State Key Laboratory of Water Environment Simulation & School of Environment, Beijing Normal University, Beijing 100875, PR China
[b] School of Geography, Beijing Normal University, Beijing 100875, PR China

ARTICLE INFO

Keywords:
Coastal squeeze
Yellow River Delta (YRD)
Coastal wetlands
Slope
Surface imperviousness

ABSTRACT

Coastal wetlands worldwide are subject to increasing threats from continued sea level rise (SLR), while their potential adaptation through land-ward migration is often impeded by natural or man-made barriers. The resultant sea- and land-ward squeeze exacerbates the loss of wetlands, causing severe ecological consequences. To address this issue for coastal wetlands at the Yellow River Delta (YRD) in China, the present study adapted a fuzzy-system-model (FSM) based coastal squeeze assessment method (Torio and Chmura, 2013) to assess the potential of coastal squeeze under assumed future SLR scenarios. Coastal squeeze indices for slope and surface imperviousness were integrated to generate the composite coastal squeeze index (CCSI) as a unified metric that accounts for both factors as the primary contributors to coastal squeeze. The distribution of the confidence-weighted CCSI was used to identify vulnerable area at three selected study sites, and results for three representative years, i.e., 1989, 2000 and 2010, were compared to illustrate the historical changes in recent decades. Due to the predominately flat topography at the YRD, slope was found to be an insignificant contributor to coastal squeeze, whereas surface imperviousness plays a dominant role. As such, the coastal squeeze potentials at the three study sites in 2000 appeared to be considerably higher than those at 1989 and 2010 as the surface imperviousness experienced increasing-then-decreasing variation arising from concurrent land cover change. The average coastal squeeze potential at the three study sites in 2000 also tended to be more sensitive to the assumed SLR scenarios, and featured a prominent peak at 1.5 m SLR. The present study showcases the assessment of coastal squeeze of wetlands at the YRD and the region, and provides important references for coastal wetland conservation efforts under increasing threats from climate change and human activities.

1. Introduction

Confronted by continuously rising sea level as well as other natural and anthropogenic stresses, coastal wetlands can transgress into adjacent uplands to increase their likelihood of survival (Kirwan and Megonigal, 2013). However, their potential landward migration can be restricted by natural and more often man-made barriers manifested as steep topography or impervious surfaces, eventually resulting in the coastal wetlands affected being squeezed into a shrinking area, i.e., the 'coastal squeeze' (Doody, 2013). Internationally, the issue of coastal squeeze has attracted growing attention, with a few attempts to assess the potential of coastal squeeze at a local scale, to assist policy making and develop adaptation strategies. Through GIS-based spatial analysis, Schleupner (2008) evaluated the coastal squeeze risk of coastal wetlands including beaches, mangrove forests, etc., in French Martinique, and identified the most vulnerable tourist destinations to the impacts of coastal squeeze. Based on landward migration opportunity and sediment budget, the risk of coastal squeeze was qualitatively categorized as low, medium and high levels. Torio and Chmura (2013) employed fuzzy system model (FSM) to make quantitative assessment of the contribution of topography and artificial shoreline protection structures to coastal squeeze in tidal wetlands. Using fuzzy logic approach, a coastal squeeze index (CSI) that varies continuously over the coastal landscape was proposed as an integrated metric to account for the effects of slope and impervious surfaces on coastal squeeze. The developed CSI was further used to assess the potential of coastal squeeze in marshes in Maine, USA and New Brunswick, Canada. Dickinson (2016) used satellite imagery to analyze historical changes in ecosystem cover, including salt marshes and mangrove communities, in a coastal region in southwest Florida. The area changes of wetlands were quantified and the main reasons for coastal squeeze were attributed to sea level rise (SLR) and highway as the landward barrier. Other local-scale coastal squeeze related studies have been performed to assess the variation of intertidal zone (Jackson and McIlvenny, 2011),

* Corresponding author.
E-mail address: ddshao@bnu.edu.cn (D. Shao).

https://doi.org/10.1016/j.ocecoaman.2017.12.018
Received 15 June 2017; Received in revised form 25 August 2017; Accepted 18 December 2017
Available online 04 January 2018
0964-5691/ © 2017 Elsevier Ltd. All rights reserved.

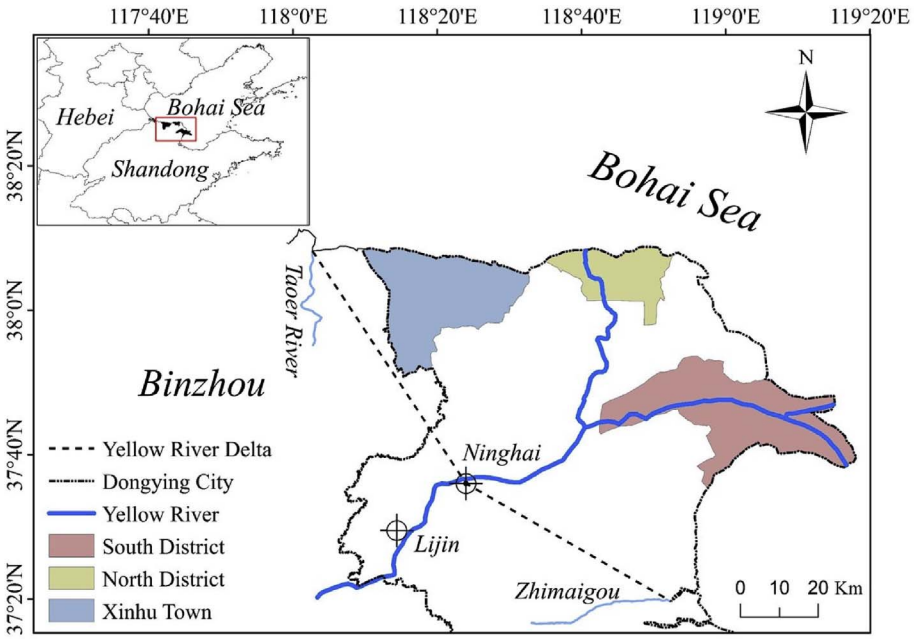

Fig. 1. The location of the Yellow River Delta and study sites.

habitat loss of loggerhead sea turtles (Mazaris et al., 2009), etc. At a regional scale, Mills et al. (2015) compared the cost of adaptation between defense and retreat in Moreton Bay, Queensland, Australia, to maintain coastal ecosystem stability under coastal squeeze. Following the local-scale assessment, Torio (2015) further extended it to continent scale and examined the relative threat of coastal squeeze throughout North America. Enwright et al. (2016) identified the landward migration corridors of coastal wetlands along the northern Gulf of Mexico coast in USA, and highlighted the importance of more robust local-scale models of landward migration in coastal squeeze mitigation planning.

As a regional economic hub where the second largest oil field of China (the Shengli Oil Field) is located and at the same time, a global ecosystem services hotspot hosting a key stopover site in the middle of the East Asian-Australasian flyway for millions of migrating birds of which many are under protection, the Yellow River Delta (YRD) is struggling to find a balance between economic development and protection of natural environment and ecosystem. In recent years, SLR and intensified human activities, e.g., hydrocarbon exploitation, upstream dam construction, land reclamation, building sea walls, etc., have caused severe land subsidence, reduced water and sediment supply, exacerbated coastal erosion (Liu et al., 2016; Ma et al., 2014; Syvitski et al., 2009; Xu et al., 2016), which further resulted in unprecedented coastal wetland degradation and loss at the YRD (Jin et al., 2016; Kuenzer et al., 2014). However, as far as we are aware, the issue of coastal squeeze resulted from the combined effects of SLR and human activities, particularly those changing the topography and surface imperviousness in area surrounding coastal wetlands, have not been studied yet, and a proper assessment is thus imperative for the conservation of valuable coastal wetlands at the YRD.

In this study, we adapted the CSI and assessment method proposed in Torio and Chmura (2013) to assess the potential of coastal squeeze of coastal wetlands at the YRD under assumed future SLR scenarios. Following Torio and Chmura (2013), we focused on the effects of slope and impervious surfaces in adjacent uplands for potential wetland migration, and developed CSI suitable for the YRD using fuzzy sigmoid function. The developed CSI was further used to evaluate the potential of coastal squeeze in three representative sites with coastal wetlands selected from the YRD, namely, the South and North Districts of the Yellow River Delta National Nature Reserve (YRDNNR) as well as Xinhu Town at Hekou District, Dongying City, and identify vulnerable area at the three study sites. The results for three representative years, i.e., 1989, 2000 and 2010, were also compared to illustrate the historical changes of coastal squeeze in the study sites, which can provide important references for coastal wetland conservation efforts under increasing threats from climate change and human activities, e.g., planning mitigation measures such as managed realignment in vulnerable areas.

The paper is organized as follows: The methodology is elaborated in Sec. 2. Specifically, the study sites and data source are introduced in Sec. 2.1 and Sec. 2.2, respectively, followed by the description of the methods to extract the potential migration uplands, slope and surface imperviousness in Sec. 2.3. The development of CSI and the uncertainty analysis are documented in Sec. 2.4 and Sec. 2.5, respectively. The primary results are presented in Sec. 3, together with the relevant discussion. The paper is concluded with the major findings obtained from the present study, as well as the recommendation for future studies.

2. Methodology

2.1. Study sites

The YRD is located in the northeast of Shandong Province, China (118°03′E – 119°20′E and 37°20′N – 38°20′N, see inset in Fig. 1). With its apex near Ninghai (118°24′E, 37°36′N), the delta extends from Taoer River estuary in the north to Zhimaigou River estuary in the south, and covers a total area of 5175 km^2 in 2000 (Fan et al., 2006). Due to the large quantity of silt carried by the Yellow River, the delta extends into the sea at a rate of 2.2 km per year with a land accretion of 3240 ha per year. The YRD is also rich in natural resources, with the second largest oil field of China (the Shengli Oil Field) situated in the delta. Industrialization and urbanization of the delta started with the oil exploitation and intensifies in recent years. At the same time, the YRD contains important wetland ecosystem, which is the habitat for numerous species, including millions of migrating birds of which many are under protection.

The YRDNNR was established in October 1992 by the State Council of China, which covers 153 000 ha land, including 58 000 ha of core zone, 13 000 ha of buffer zone and 82 000 ha of experimental zone. As a wetland-type reserve, it was established to protect the newly formed wetland ecosystem as well as rare and endangered birds. The reserve was divided into two districts: the South District located at the present

Table 1
Data inventory.

Data	Source	Format	Time	Resolution	Purpose
SRTM DEM	CGIAR-CSI	tif	2000	90 m	slope
Landsat imagery	USGS	tif	1989-03-09, 2000-05-02, 2010-09-11	30 m	impervious surfaces
Land cover	Hua et al. (2016)	shp	1989, 2000, 2010	vector	the range of elevation of the vegetation distribution area

Table 2
The range of elevation of the vegetation distribution area for each study site in each year (m).

Year	Study sites		
	South District	North District	Xinhu Town
1989	2.36–3.67	0.36–1.39	3.36–4.11
2000	−0.64–1.30	0.36–1.41	1.36–2.38
2010	0.36–1.10	0.36–1.35	1.36–1.83

* The vertical datum for the DEMs used in our study was 1985 National Elevation Datum, China.

estuary of the Yellow River with a total area of 104 500 ha, and the North District lies in the former estuary (before 1976) with a total area of 48 500 ha. In 2014, 95 949.9 ha of wetlands in the YRDNNR have been designated as international Ramsar site.

We selected three representative sites with coastal wetlands from the YRD, namely, the South and North Districts of the YRDNNR (hereinafter referred to as South District and North District), as well as Xinhu Town at Hekou District, Dongying city, as the study sites to assess the potential of coastal squeeze under assumed future SLR scenarios. The vegetated coastal wetlands of the YRD are mainly distributed in the South and North Districts, which are the most vital area in the context of coastal squeeze. Xinhu Town is located at the far west of Dongying City bordering Binzhou City, geographically separated from the South and North Districts. At the same time, it is an area with rich resources of oil, gas and bittern, and is thus concentrated with industrial activities and contrasts with the South and North Districts in land use and land cover features. As such, Xinhu Town was selected to ensure the diversity and representativeness of the study sites, and improve the quality and applicability of the CSI thus developed. The location of the study sites is illustrated in Fig. 1.

2.2. Data sets

Data used in this study mainly consisted of slope, impervious surfaces and land cover data, which are listed in Table 1.

(1) Slope. We downloaded the 90 m-resolution SRTM DEM data from the CGIAR-CSI website (srtm.csi.cgiar.org/SELECTION/inputCoord.asp). Following basic preprocessing such as projecting the images into the Albers Conical Equal Area and calibrating the vertical datum to the 1985 National Elevation Datum, China, the downloaded DEM data were used to calculate the slopes in ArcGIS 10.2.
(2) Impervious surfaces. We used the Landsat TM and ETM + level 1 products of the YRD from the Landsat satellite images module of the USGS website (http://landsatlook.usgs.gov/viewer.html). Landsat satellite imagery has a high resolution and a variety of formats. We chose the good-quality Landsat images of the YRD without cloud cover as the primary data for extracting impervious surfaces.
(3) Land use data. The land use data reported in Hua et al. (2016) was used to extract the range of elevation of the vegetation distribution area of the three study sites.

2.3. Potential migration uplands, slope and impervious surfaces

We extracted salt marsh from the land use data for each year as the vegetation distribution area at the YRD for that year. The respective range of elevation of the vegetation distribution area for each study site was obtained by overlaying the land use data layer over the DEM data layer in ArcGIS 10.2. 95% confidence interval and the quantiles of the original ranges were selected to rule out the sporadic outliers in SPSS 22.0 and obtain the final range of elevation (see Table 2).

Using the range of elevation of the vegetation distribution area relative to the current sea level (*h1*) for each site (Table 2), we determined the area below the upper limit of the vegetation distribution area from the DEM data (termed Marsh0). Under the assumed SLR, the associated potential migration uplands could be identified as illustrated

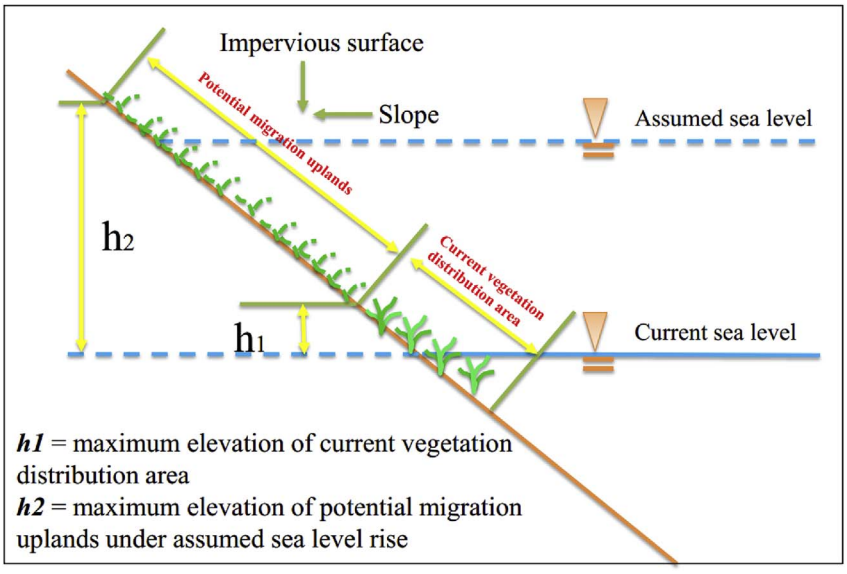
Impervious surface
Slope
Assumed sea level
Potential migration uplands
Current vegetation distribution area
h2
h1
Current sea level
h1 = maximum elevation of current vegetation distribution area
h2 = maximum elevation of potential migration uplands under assumed sea level rise

Fig. 2. Schematic showing the potential migration uplands under assumed sea level rise.

Fig. 3. Potential migration uplands at Xinhu Town under 2.5 m sea level rise in (a) 1989, (b) 2000, (c) 2010.

in the schematic diagram in Fig. 2. We first set the maximum SLR as 2.5 m, and the inundated area was termed Marsh250. Subtracting Marsh250 by Marsh0 yielded the resultant potential migration uplands (refer to as '*upland*' hereinafter) (Fig. 3). We further considered 0.5 m, 1.0 m, 1.5 m, 2.0 m and 2.5 m SLR to compare different potential migration uplands under different SLR scenarios.

The slope in the study sites was calculated on 3 × 3 moving grids of the DEM data using the formula reported in Burrough and McDonell (1998). Landsat images consist of seven spectral bands: bands 1, 2 and 3 are blue-green, green and red light, respectively, in visible spectra; band 4 is near-infrared and can be related to the vegetation biomass; band 5 and 7 are middle infrared; band 6 is thermal infrared and can be related to the thermal radiation ability of the surface features (USGS, 1998). In view of the relatively high thermal radiation ability of impervious surfaces, Xu (2008) proposed to use the ratio between band 6 and band 4 to distinguish impervious surfaces from vegetated area, and then rule out the remaining sand, soil and water body by further examining bands in infrared and visible spectra, i.e., bands 5 and 1, 2 or 3. The above integrated use of multiple bands led to the normalized difference impervious surface index (NDISI) defined as follows,

$$\mathrm{NDISI} = \frac{\mathrm{TIR} - (\mathrm{VIS} + \mathrm{NIR} + \mathrm{MIR})/3}{\mathrm{TIR} + (\mathrm{VIS} + \mathrm{NIR} + \mathrm{MIR})/3} \quad (1)$$

in which TIR represents band 6 (thermal infrared); VIS represents any of the three bands in visible spectra (band 1 to 3), and band 2 (green) was adopted in this study; NIR represents band 4 (near-infrared); MIR represents band 5 (middle infrared).

Since the albedo of water is lower than that of impervious surfaces, the resultant noise will adversely affect the NDISI result. To mitigate this effect, we replaced the visible band with the modified normalized water index (MNDWI) proposed in Xu (2008). Performing the above band operations on the downloaded Landsat 5 or 7 satellite images of

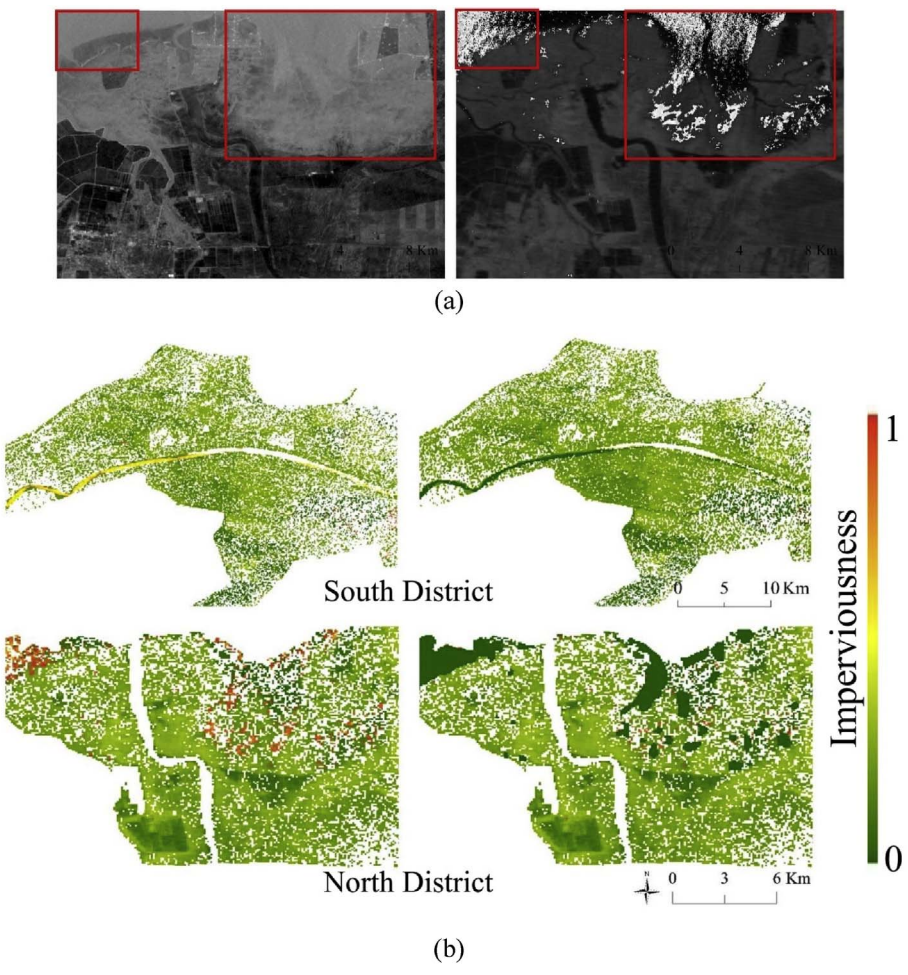

Fig. 4. (a) The Landsat image (left) and the normalized NDISI result (right) at North District in 2010; (b) The distribution of the normalized NDISI in the potential uplands at South District and North District before (left) and after (right) adjustment in 2010.

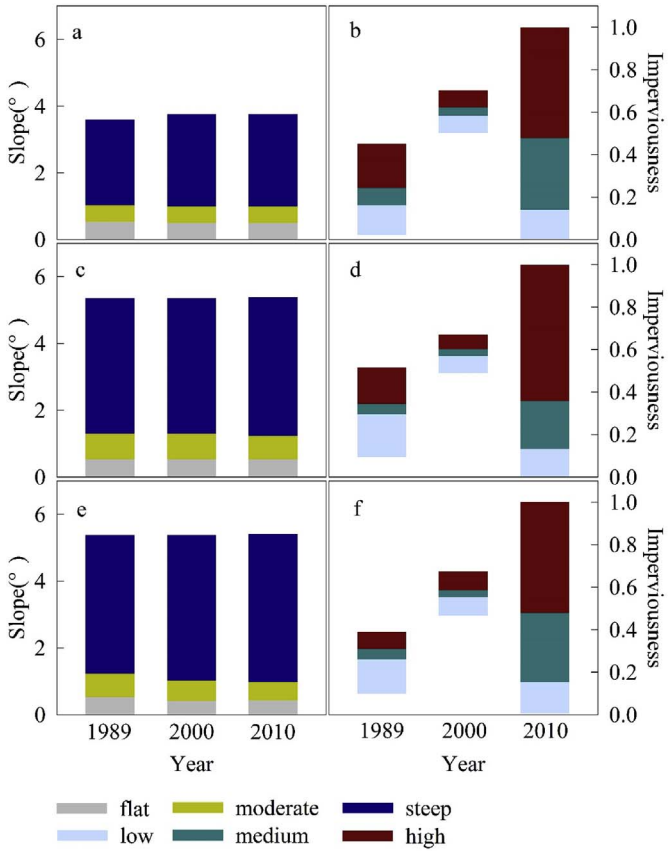

Fig. 5. Classification of slope and normalized NDISI in the potential migration uplands of the three study sites: (a) and (b) South District, (c) and (d) North District, (e) and (f) Xinhu Town in 1989, 2000 and 2010.

Table 3
The average of the normalized NDISI in the potential migration uplands of the three study sites throughout the three years for different classes and the associated squeeze potential.

Classes	1989	2000	2010	Average	Squeeze Potential
low	0.07–0.24	0.49–0.57	0.00–0.14	0.32	0.00
medium	0.24–0.30	0.57–0.60	0.14–0.44	0.44	0.50
high	0.30–0.45	0.60–0.68	0.44–1.00	0.71	1.00

the YRD in ENVI5.0 yielded the NDISI. In principle, the NDISI value indicates the imperviousness of the surface, i.e., a higher NDISI value represents a more impervious surface, and vice versa. However, the calculated NDISI value varies from −1 to 1, and to facilitate the development of the CSI, a proper normalization to cap it between 0 and 1 seems necessary. We adopted the following normalization to achieve this purpose,

$$Nimper = \frac{imper - \text{minimper}}{\text{maximper} - \text{minimper}} \quad (2)$$

where *N_imper* and *imper* denote normalized and original NDISI, respectively, while *max_imper* and *min_imper* denote the maximum and minimum NDISI attained in the results of the three years. As shown in Fig. 4b, as the color changes from green to red in the map, the associated normalized NDISI varies from 0 to 1, i.e., from least impervious to most impervious. Notably, high-imperviousness patches were identified surrounding the old estuary at North District. However, after scrutinizing the Landsat image, we recognized the patches as sediment plumes (Fig. 4a). As such, we adjusted the relevant normalized NDISI to a value very close to 0 and updated the map of surface imperviousness (Fig. 4b). Similar adjustments were made along the current course of the Yellow River at South District. We also resampled the 30 m resolution surface imperviousness data to match the 90 m resolution slope data to achieve consistent grid size.

2.4. Development of the CSI

Torio and Chmura (2013) employed fuzzy sigmoid function to relate slope and surface imperviousness to the potential of coastal squeeze, and form the respective CSI. In this study, since the terrain is predominantly flat throughout the YRD, and the maximum slope in the potential migration uplands of the three study sites is merely 5.41°, fuzzy sigmoid function fitted using this biased slope dataset would result in unrealistic CSI for slope. As such, we adopted the fuzzy sigmoid function for slope from Torio and Chmura (2013), and only fit the fuzzy sigmoid function for surface imperviousness. For surface imperviousness, the fuzzy sigmoid function reads,

$$\mu = \frac{1}{1 + \left(\frac{N.imper}{midpoint}\right)^{-spreadparameter}} \quad (3)$$

where μ denotes the fuzzy squeeze variable; *midpoint* denotes the assumed midpoint of the distribution of surface imperviousness throughout the study sites for the study period; *spreadparameter* denotes the unknown spread parameter in the fuzzy sigmoid function. The expression of the fuzzy sigmoid function for slope is similar.

We then classified the distribution of slope and surface imperviousness in the potential migration uplands of each study site into three classes using Jenks (1967)'s classification (Fig. 5). The distributions of the slope shown in Fig. 5 confirm that the slope at the three

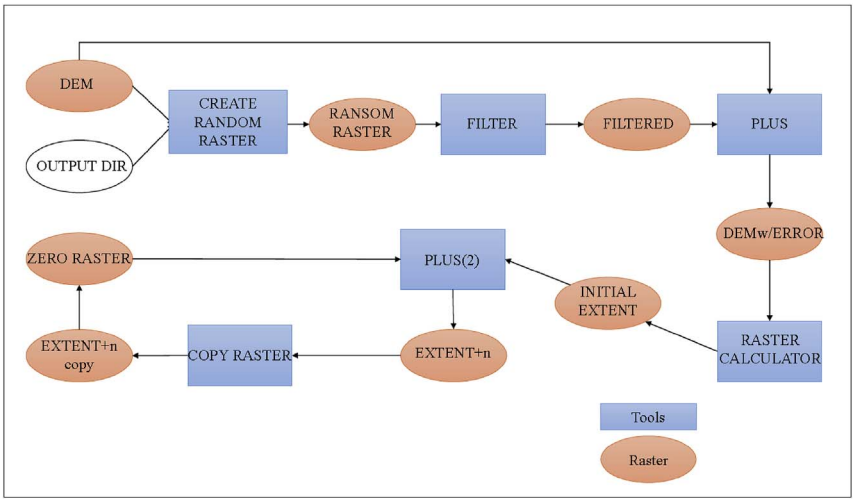

Fig. 6. Implementation of the uncertainty model in ArcGIS ModelBuilder.

study sites throughout the three years is consistently low. The distributions of the surface imperviousness were used to compute the average of the normalized NDISI of the three study sites throughout the three years for different classes, which were further used to fit the fuzzy sigmoid function (Table 3). Notably, the average of each class was based on the upper bounds of the class, and the average of the medium class of the three sites throughout the three years (0.44) was assumed as the *midpoint* in Eq. (3) with a squeeze potential of 0.5. The *spreadparameter* in Eq. (3) was further determined by assuming that the maximum imperviousness, i.e., 0.71, corresponded to a squeeze potential very close to 1, e.g., 0.95. The resultant *spreadparameter* was 6.29. Substituting the derived *midpoint* and *spreadparameter* into Eq. (3) led to the CSI for surface imperviousness. As mentioned above, the CSI for slope was rendered using the fuzzy sigmoid function with *midpoint* (11.5°) and *spreadparameter* (3.95) from (Torio and Chmura, 2013).

We then integrated the computed CSI for slope and surface imperviousness, and adopted the larger value of the two to represent the composite CSI (CCSI) at the point of interest. The above fuzzy operations were carried out in ArcGIS to compute the CCSI in the potential migration uplands of the three study sites.

2.5. Uncertainty analysis

As stated in Torio and Chmura (2013), the 'bathtub' type of inundation model adopted in this study to simulate the SLR scenarios is appropriate only when the relevant uncertainty is properly addressed. Following their study, we built an uncertainty model based on Monte Carlo simulation in ArcGIS to account for the confidence of locating the potential migration uplands given the uncertainty in DEM and range of elevation of vegetation distribution area (Fig. 6). The result of the uncertainty model is a map showing the distribution of probability that the individual pixel of the inundated DEM falls in the specified elevation range. Multiplying the probability (confidence level) to the computed CCSI results in the confidence-weighted CCSI. The details of the uncertainty model can be found in Torio and Chmura (2013), and are not repeated here for brevity.

3. Results and discussion

Fig. 7 shows the distribution of slope at the YRD. As mentioned above, the YRD is very flat as illustrated by predominantly green area with sporadic red patches denoting area with mild slope. The maximum slope throughout the YRD is only 8.67°, and the maximum slope in the potential migration uplands is only 5.41°.

The distributions of the normalized NDISI at South District for the three years are shown in Fig. 8. While the normalized NDISI value increases significantly from 1989 to 2000, it falls back in the following decade. The history of change in the surface imperviousness is consistent with the land cover change. It was reported that, from 1995 to 1999, the areas of both the natural and constructed wetland decreased significantly (Liu et al., 2010). Since 2000, however, many farmland have been converted to water bodies and constructed wetlands (Hong et al., 2016). These changes partly explain the increasing-then-decreasing surface imperviousness. Note also that only the colored areas in the various maps are the potential migration uplands.

Fig. 9 presents the CSI for surface imperviousness and slope. It shows that the maximum slope (5.41°) in the potential migration uplands of the three study sites throughout the three years corresponds to a slim squeeze potential of 0.05, confirming the minimal contribution of slope to the coastal squeeze at the YRD. Table 4 shows the average CCSI of the three study sites in the three years. Consistent with the surface imperviousness variation, the average CCSI increases to above 0.8 in 2000 and drops back to below 0.1 in 2010.

The uncertainty analysis results (the confidence level) under 0.5 m, 1.0 m, 1.5 m, 2.0 m and 2.5 m SLR at South District in 2000 were plotted in Fig. 10. The distribution of the confidence level moves gradually inland with increasing SLR, indicating the movement of the potential migration uplands under different SLR scenarios. The average confidence level shows a steadily decreasing trend with increasing SLR.

The distributions of the confidence-weighted CCSI in the potential migration uplands under 0.5 m, 1.0 m, 1.5 m, 2.0 m and 2.5 m SLR in the three years are shown in Fig. 11. In general, as the vegetation distribution area for each study site shifts towards lower altitude from 1989 to 2010 (Table 2), the corresponding uplands expands (see Fig. 3

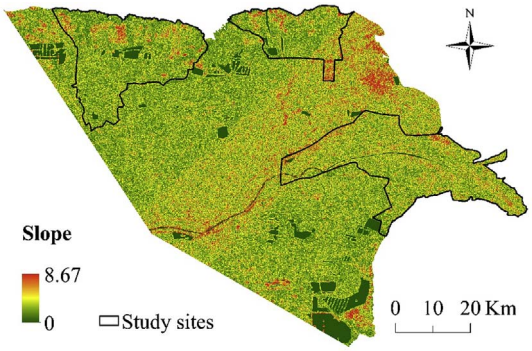

Fig. 7. The distribution of slope at the Yellow River Delta.

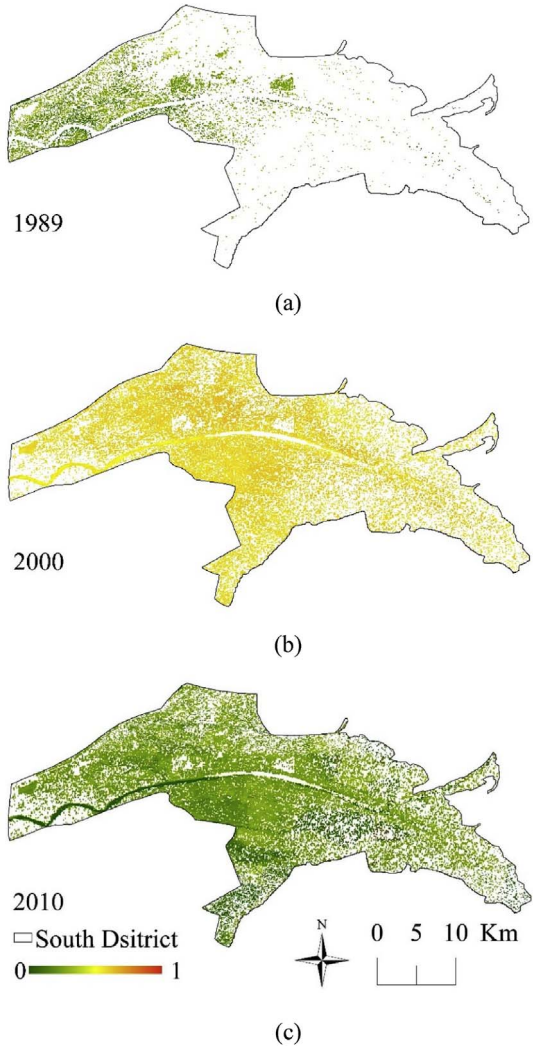

Fig. 8. The distribution of the normalized NDISI value at South District in (a) 1989, (b) 2000, (c) 2010.

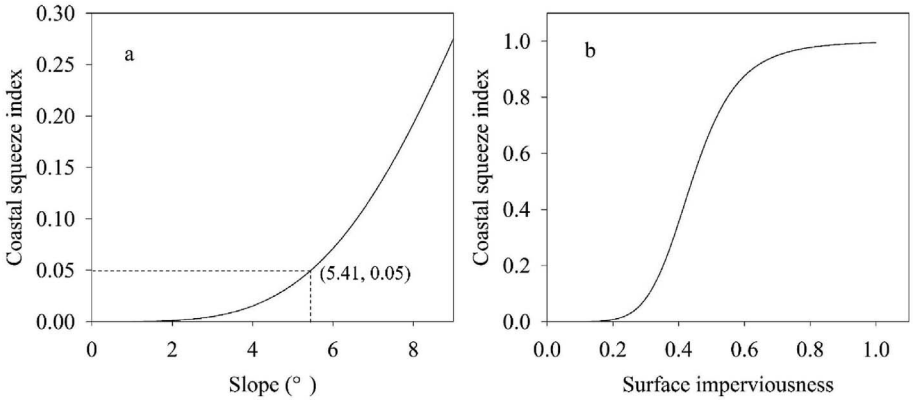

Fig. 9. Fuzzy sigmoid function curve showing the correlation between (a) slope and (b) surface imperviousness and the respective coastal squeeze index.

Table 4
Average composite coastal squeeze index (CCSI) of the three study sites in the three years.

Year	South District	North District	Xinhu Town
1989	0.03	0.13	0.09
2000	0.88	0.86	0.85
2010	0.03	0.03	0.02

for Xinhu Town), suggesting more suitable areas to accommodate inland migration in 2010. As shown in Fig. 11, as the color changes from green to red, the squeeze potential changes from lowest to highest. Meanwhile, the vulnerable areas (red) with higher confidence-weighted CCSI move gradually inland. Among the different SLR scenarios, the overall coastal squeeze potential of the three study sites in 2000 appears to increase with increasing SLR in the range of 0.5 m–1.5 m, and the trend reverses beyond 1.5 m, which is presumably due to the effects of the distribution of confidence level relative to the distribution of CCSI. Whereas the squeeze potential of the three study sites attain low value, and the distributions remain largely unchanged among different SLR scenarios in 1989 and 2010.

The average coastal squeeze potential at the three study sites under different SLR scenarios are presented in Fig. 12. Consistent with the variation of the overall distributions, the average coastal squeeze potential at the three study sites in 2000 all peaks at 1.5 m, with the highest peak of 0.64 at South District. By contrast, the squeeze potential in 1989 and 2010 is considerable smaller, and ranges from 0 to 0.08. The contrast is presumably attributed to the change in surface imperviousness discussed above.

It is worth pointing out that, the average coastal squeeze potentials for Xinhu Town, which is with higher population density and urbanization level, are unexpectedly not the greatest among the three study sites. The abundant water bodies, e.g., four rivers winding through the town, and the widespread shallow sea and salt ponds may partly contribute to the reduced squeeze potentials (Fig. 13).

As mentioned above, the predominantly flat terrain throughout the YRD makes slope a less important contributor to coastal squeeze. Hence, we explored neglecting the effect of slope altogether, and considering only the contribution of surface imperviousness to coastal squeeze (termed confidence-weighted coastal squeeze index for imperviousness (CSII)). The average CSII at the three study sites for the three years under different SLR scenarios are presented along with the corresponding CCSI in Fig. 12, and the difference is hardly discernible. We further subtracted the confidence-weighted CSII from the confidence-weighted CCSI using raster calculator, and found the difference to be consistently close to zero throughout the domain, confirming that neglecting the contribution of topography in the assessment of coastal squeeze in a predominantly flat area like the YRD is legitimate.

4. Conclusion

The present study adapted the fuzzy-system-model-based coastal squeeze assessment method proposed by Torio and Chmura (2013) to assess the potential of coastal squeeze of three study sites, namely, the

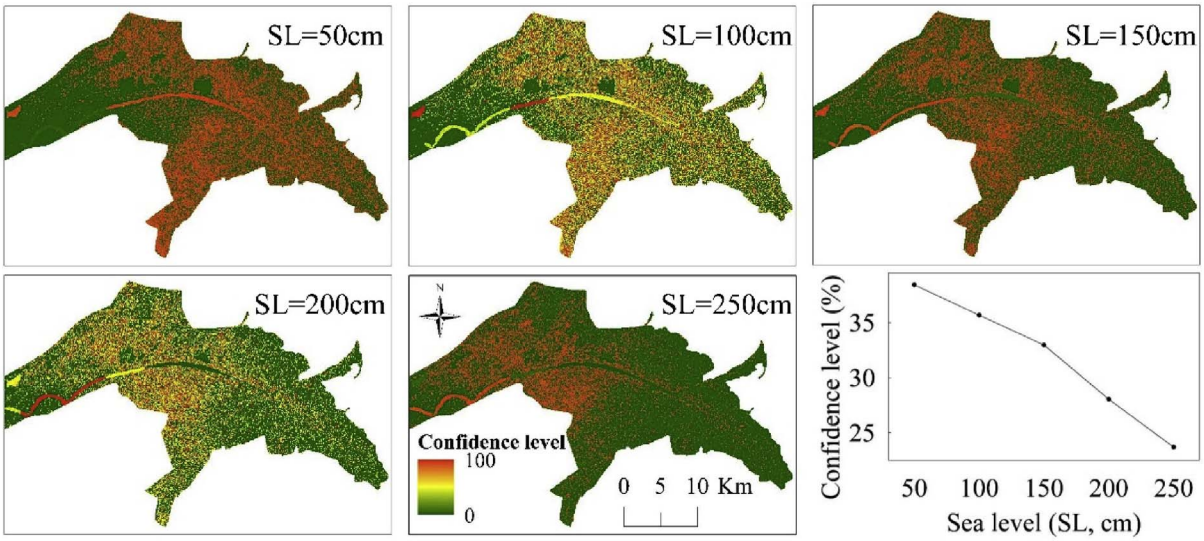

Fig. 10. The distribution and average of the confidence level at South District in 2000.

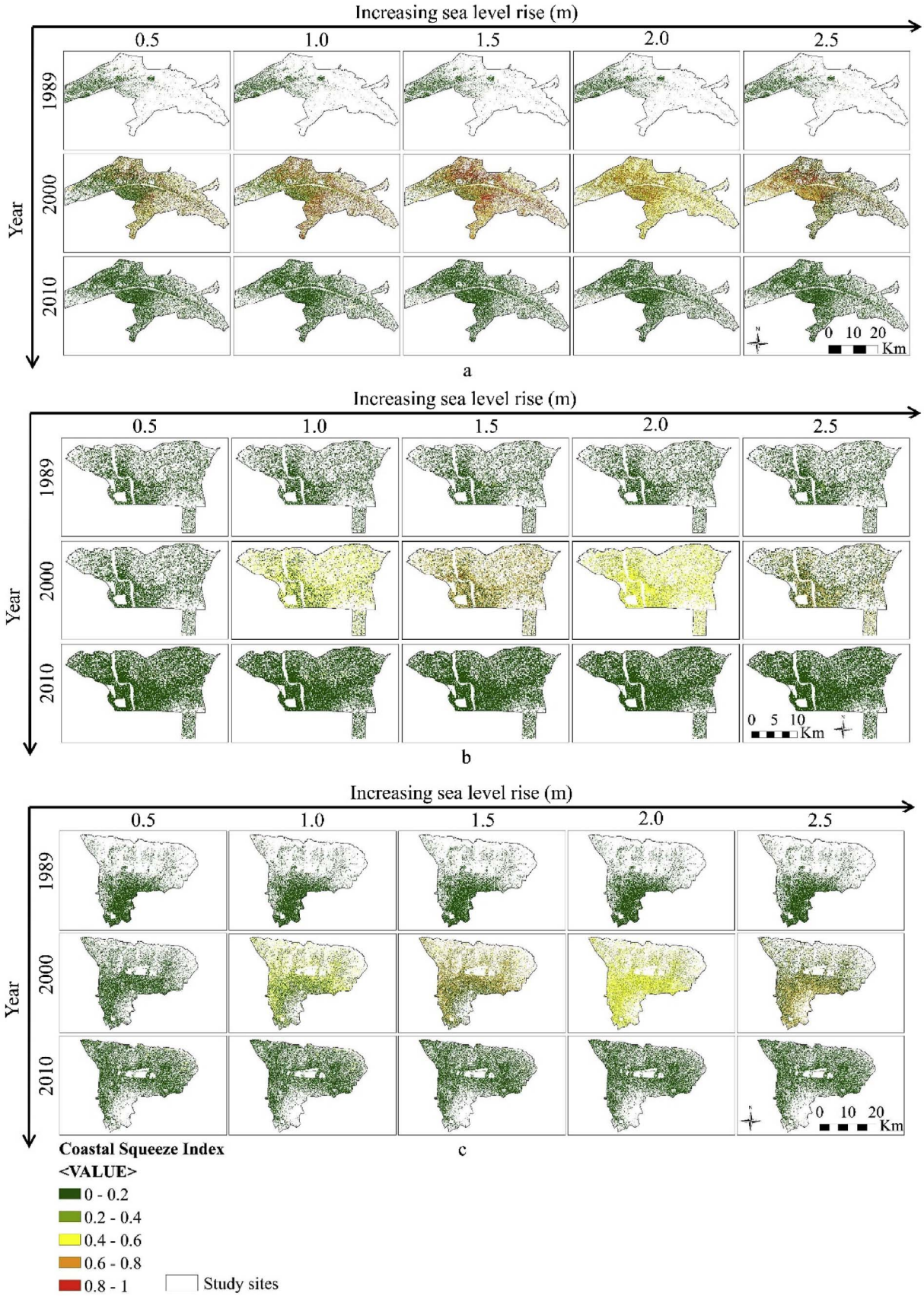

Fig. 11. The distributions of the confidence-weighted composite coastal squeeze index in the potential migration uplands of the three study sites: (a) South District, (b) North District, (c) Xinhu Town in 1989, 2000 and 2010.

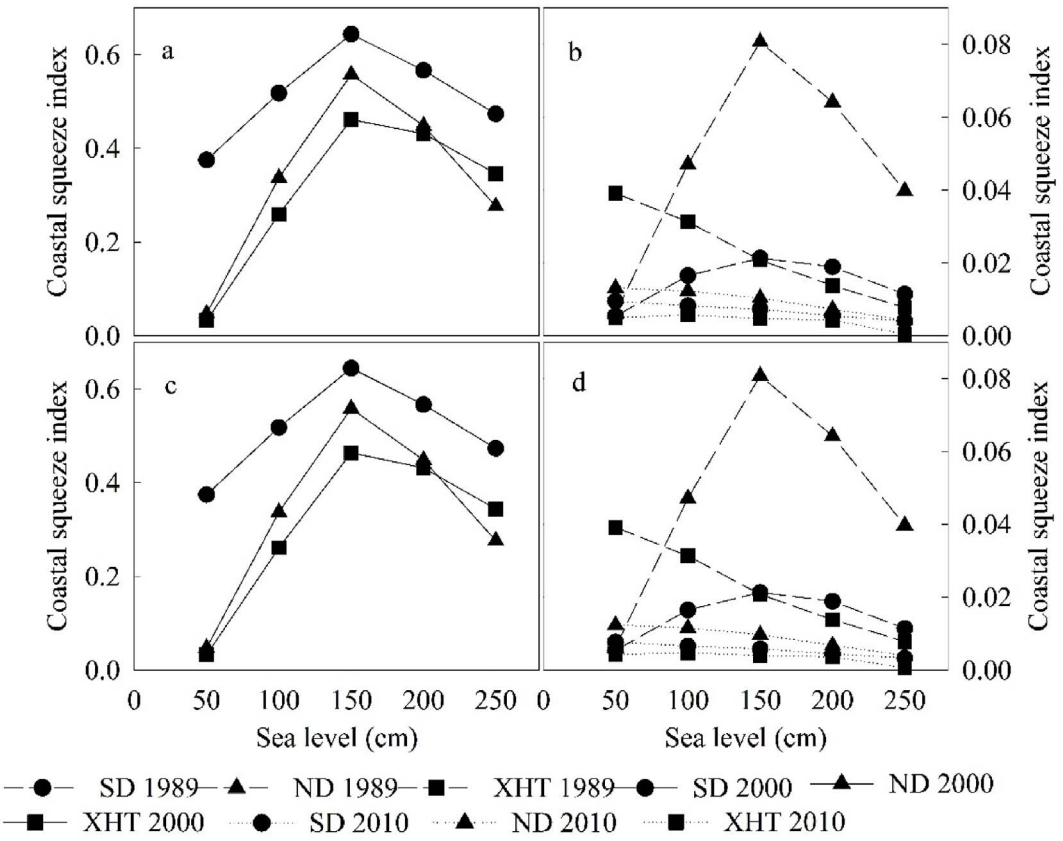

Fig. 12. The average coastal squeeze index at the three study sites for the three years under different sea level rise scenarios: (a) and (b) confidence-weighted composite coastal squeeze index (CCSI), (c) and (d) confidence-weighted coastal squeeze index for imperviousness (CSII).

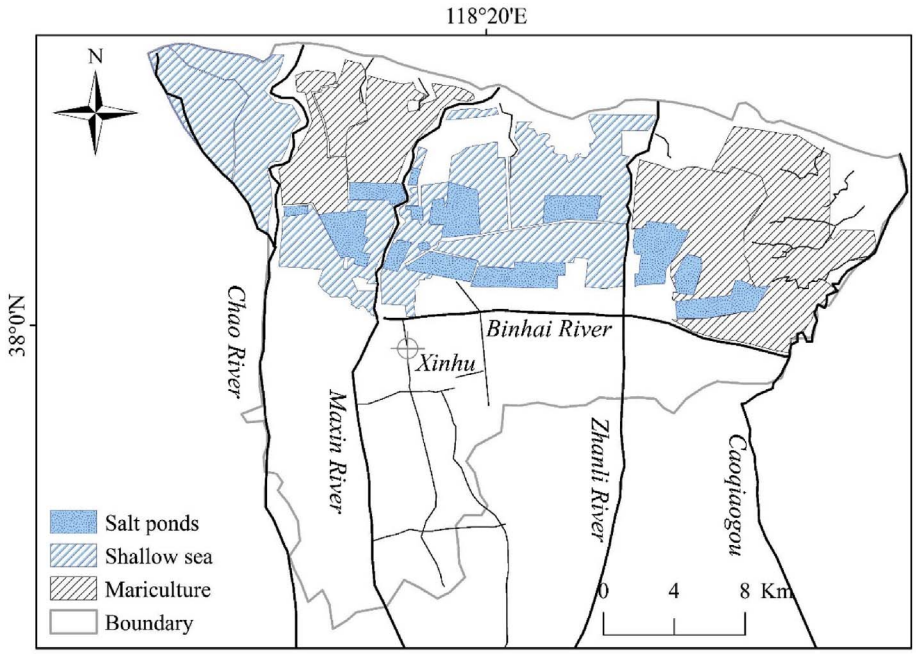

Fig. 13. Distribution of water bodies at Xinhu Town.

South and North Districts of the Yellow River Delta National Nature Reserve as well as Xinhu Town at Hekou District, Dongying City, at the Yellow River Delta under assumed future SLR scenarios in 1989, 2000 and 2010. The major findings from the present study are as follows:

(1) Due to the predominately flat topography at the Yellow River Delta, slope was found to be an insignificant contributor to coastal squeeze, whereas surface imperviousness plays a dominant role. The distribution of confidence-weighted coastal squeeze index for imperviousness appeared to almost coincide with the confidence-weighted composite coastal squeeze index, which suggests that future assessment at the YRD or areas with similar topography can

safely use coastal squeeze index for imperviousness to save the time and effort.

(2) Among the three years representative of three recent decades, the coastal squeeze potentials at the three study sites in 2000 appeared to be considerably higher than those at 1989 and 2010 as the surface imperviousness experienced increasing-then-decreasing variation arising from concurrent land cover change. Among the different SLR scenarios, the coastal squeeze potential at the three study sites in 2000 also tended to be more sensitive to the assumed SLR scenarios and featured a prominent peak at 1.5 m SLR, whereas the distributions of coastal squeeze potential remain largely unchanged among different SLR scenarios in 1989 and 2010.

(3) Apart from the land cover change, the distribution of water bodies in the study sites can strongly affect the potential of coastal squeeze. Among the three study sites, the average coastal squeeze potentials at Xinhu Town, which is with higher population density and urbanization level, are unexpectedly not the greatest, presumably due to the widespread water bodies including rivers, shallow sea and salt ponds.

As a preliminary assessment, only publicly available SRTM DEM (90 m-resolution) and Landsat TM and ETM+ (30 m-resolution) data were used in our study. More accurate assessment incorporating higher resolution Lidar and land use data will be of interest in the future.

Acknowledgements

This work was supported by the National Key Basic Research Program of China (973 Program) (Grant No. 2013CB430402) and the Fundamental Research Funds for the Central Universities (Grant No. 2015KJJCB20). Useful discussion with Mr. Weilun Gao on uncertainty model building is also acknowledged. The authors appreciate the constructive comments and suggestions from the two anonymous reviewers on an earlier version of the manuscript.

References

Burrough, P.A., McDonell, R.A., 1998. Principles of Geographical Information Systems. Oxford University Press, New York.

Dickinson, D.M., 2016. Spatial Analysis of Historic Coastal Squeeze on Mangroves and Other Wetlands in Southwest Florida. MS Thesis. Florida Gulf Coast University.

Doody, J.P., 2013. Coastal squeeze and managed realignment in southeast England, does it tell us anything about the future? Ocean Coast. Manag. 79, 34–41. http://dx.doi.org/10.1016/j.ocecoaman.2012.05.008.

Enwright, N.M., Griffith, K.T., Osland, M.J., 2016. Barriers to and opportunities for landward migration of coastal wetlands with sea-level rise. Front. Ecol. Environ. 14, 307–316.

Fan, H., Huang, H., Zeng, T., 2006. Impacts of anthropogenic activity on the recent evolution of the Huanghe (Yellow) River Delta. J. Coast. Res. 22, 919–929.

Hong, J., Lu, X., Wang, L., 2016. Quantitive analysis of the factors driving evolution in the Yellow River Delta Wetland in the past 40 years. Ecologica 36, 924–935.

Hua, Y., Cui, B., He, W., Cai, Y., 2016. Identifying potential restoration areas of freshwater wetlands in a river delta. Ecol. Indic. 71, 438–448.

Jackson, A.C., McIlvenny, J., 2011. Coastal squeeze on rocky shores in northern Scotland and some possible ecological impacts. J. Exp. Mar. Biol. Ecol. 400, 314–321. http://dx.doi.org/10.1016/j.jembe.2011.02.012.

Jenks, G.F., 1967. The Data Model Concept in Statistical Mapping. International Yearbook of Cartography 7.

Jin, Y., Yang, W., Sun, T., Yang, Z., Li, M., 2016. Effects of seashore reclamation activities on the health of wetland ecosystems: a case study in the Yellow River Delta, China. Ocean Coast. Manag. 123, 44–52.

Kirwan, M.L., Megonigal, J.P., 2013. Tidal wetland stability in the face of human impacts and sea-level rise. Nature 504, 53–60. http://dx.doi.org/10.1038/nature12856.

Kuenzer, C., Ottinger, M., Liu, G.H., Sun, B., Baumhauer, R., Dech, S., 2014. Earth observation-based coastal zone monitoring of the Yellow River Delta: dynamics in China's second largest oil producing region over four decades. Appl. Geogr. 55, 92–107. http://dx.doi.org/10.1016/j.apgeog.2014.08.015.

Liu, Y., Huang, H., Liu, Y., Bi, H., 2016. Linking land subsidence over the Yellow River delta, China, to hydrocarbon exploitation using multi-temporal InSAR. Nat. Hazards 84, 1–21.

Liu, Y., Zhang, J., Ma, Y., Shan, K., 2010. Changes of wetland landscape pattern in Eastern Yellow River delta nature reserve from 1995 to 1999. J. Appl. Ecol. 21, 2904–2911.

Ma, Z., Melville, D.S., Liu, J., Chen, Y., Yang, H., Ren, W., Zhang, Z., Piersma, T., Li, B., 2014. Rethinking China's new great wall. Science (80-.) 346, 912–914.

Mazaris, A.D., Matsinos, G., Pantis, J.D., 2009. Evaluating the impacts of coastal squeeze on sea turtle nesting. Ocean Coast. Manag. 52, 139–145.

Mills, M., Leon, J.X., Saunders, M.I., Bell, J., Liu, Y., O'Mara, J., Lovelock, C.E., Mumby, P.J., Phinn, S., Possingham, H.P., 2015. Reconciling development and conservation under coastal squeeze from rising sea-level. Conserv. Lett. 9 (5), 361–368.

Schleupner, C., 2008. Evaluation of coastal squeeze and its consequences for the Caribbean island Martinique. Ocean Coast. Manag. 51, 383–390. http://dx.doi.org/10.1016/j.ocecoaman.2008.01.008.

Syvitski, J.P.M., Kettner, A.J., Overeem, I., Hutton, E.W.H., Hannon, M.T., Brakenridge, G.R., Day, J., Vörösmarty, C., Saito, Y., Giosan, L., 2009. Sinking deltas due to human activities. Nat. Geosci. 2, 681–686.

Torio, D.D., 2015. Modeling the Impacts of Sea Level Rise on Tidal Wetlands. PhD Thesis. McGill University.

Torio, D.D., Chmura, G.L., 2013. Assessing coastal squeeze of Tidal Wetlands. J. Coast. Res. 29, 1049–1061. http://dx.doi.org/10.2112/jcoastres-d-12-00162.1.

USGS, 1998. Landsat 7 Science Data Users Handbook. Gen. Interes. Publ.

Xu, H., 2008. A new remote sensing index for fastly extracting impervious surface information. Geomat. Inf. Sci. Wuhan Univ. 33 (11) 1150–1153.

Xu, X., Li, X., Chen, M., Li, X., Duan, X., Zhu, G., Zhe, F., Ma, Z., 2016. Land-ocean-human interactions in intensively developing coastal zone: demonstration of case studies. Ocean Coast. Manag. 133, 28–36. http://dx.doi.org/10.1016/j.ocecoaman.2016.09.006.